Mesoscale DVC analyses and parameter calibration for pantographic block in 3-point flexure

Malo Valmalle, Benjamin Smaniotto, Mario Spagnuolo, Alessandro Ciallella, François Hild

Mesoscale DVC analyses and parameter calibration for pantographic block in 3-point flexure

Malo Valmalle[a,b], Benjamin Smaniotto[a,b], Mario Spagnuolo[c,d,*], Alessandro Ciallella[d,e] and François Hild[a]

[a]ENS Paris-Saclay, DGM–Department of Mechanical Engineering, Gif-sur-Yvette, France
[b]Université Paris-Saclay, CentraleSupélec, ENS Paris-Saclay, CNRS LMPS–Laboratoire de Mécanique Paris-Saclay, Gif-sur-Yvette, France
[c]DICAAR (Department of Civil and Environmental Engineering and Architecture), University of Cagliari, Cagliari, Italy
[d]M&MoCS (International Research Center for the Mathematics and Mechanics of Complex Systems), University of L'Aquila, L'Aquila, Italy
[e]DICEAA (Department of Civil, Construction-Architectural and Environmental Engineering), University of L'Aquila, L'Aquila, Italy

ARTICLE INFO

Keywords:
Digital Volume Correlation (DVC)
Metamaterial
Backtracking
Generalized Continua

ABSTRACT

In the present work, the mechanical response of a fiber network metamaterial was studied when subjected to 3-point flexure. To account for the initial deformation of the sample due to the fabrication process, backtracking (*i.e.,* the nominal mesh was accurately repositioned in the reference configuration) was implemented in the Digital Volume Correlation (DVC) procedure. Kinematic fields were then measured via DVC at two different scales. Finite element based DVC was validated thanks to a series of initialization steps. The displacement fields were successfully measured and a peculiar deformation mechanism was observed. These measurements were employed to calibrate the constitutive parameters of a second gradient continuum model introduced for modeling this type of metamaterial. Numerical simulations are shown to be in good agreement with experimental measurements at the macroscopic scale.

1. Introduction

The advancement of additive manufacturing techniques has made it possible to develop metamaterials whose inner architecture may be very complex (Schaedler and Carter, 2016; Pfaff, Bierdel, Hoschke, Wickert, Riedel and Hiermaier, 2020). This complexity determines their mechanical properties, which can be designed to be highly-performing and not achievable with standard materials. Such remarkable properties may persist when new mesostructures are embedded in a matrix. The obtained composite material, which can be regarded as a fiber reinforced matrix (Franciosi, 2020; Schulte, Dittmann, Eugster, Hesch, Reinicke, dell'Isola and Hesch, 2020), still maintains some of the peculiarities of the underlying metamaterial architecture.

Whether considered as an (embedded) phase of a composite material or as a material *per se*, the mechanics of metamaterials is often modeled in the context of generalized continua models (Alibert, Seppecher and dell'Isola, 2003). In the class of mechanical metamaterials, a very sophisticated one is represented by fibrous arrangements (*i.e.,* architectures composed of fiber layers variously interconnected (Ciallella, Pasquali, Gołaszewski, D'Annibale and Giorgio, 2021; Spagnuolo and Cazzani, 2021)). When designing fibrous metamaterials, a fundamental property to exploit is the fact that the morphology of their mesostructure significantly influences their macroscopic response (Yang, Ganzosch, Giorgio and Abali, 2018). These properties are controlled to a lesser extent by the microscopic properties of the constituent material (Spagnuolo, Peyre and Dupuy, 2019). Therefore, by working only on the geometric arrangement of basic structural elements, and without changing the constitutive material, it is possible to obtain very different macroscopic responses (Giorgio, 2016; Boutin, dell'Isola, Giorgio and Placidi, 2017).

There exist natural materials in which the aforementioned principle is exploited. Remarkable examples of natural fibrous architectures are found in bone tissues or woods. In the case of bone tissues, the architecture of the fiber network is obtained through the process of topological optimization (Desmorat and Desmorat, 2008; Giorgio, 2021) induced by natural evolution. In this way, the resulting bone microstructure is the best possible for finding a material having optimal ratios between resistance and weight (George, Allena and Remond, 2018; Giorgio, dell'Isola, Andreaus, Alzahrani, Hayat and Lekszycki, 2019).

In this paper, results are presented concerning a 3-point flexural test performed on a specimen made of a fibrous architecture known as pantographic metamaterial. The simplest example of such metamaterial is a sheet composed of two mutually orthogonal fiber layers mechanically interconnected by cylindrical joints. These joints are generally referred to as pivots or hinges in the literature (Alibert et al., 2003; dell'Isola, Giorgio, Pawlikowski and Rizzi, 2016; Giorgio, Varano, dell'Isola and Rizzi, 2021). They either have some torsional rigidity, and thus add a deformation mechanism to the fibers, or behave as perfect hinges, thereby only ensuring that the families of fibers remain mutually bonded, but exerting no constraint on the relative rotations between them (Valmalle, Vintache, Smaniotto, Gutmann, Spagnuolo, Ciallella and Hild, 2022). The relevance of such

*Corresponding author
mario.spagnuolo@unica.it (M. Spagnuolo)
ORCID(s): 0000-0003-1248-1318 (M. Valmalle); 0000-0003-2614-3328 (M. Spagnuolo); 0000-0001-8188-5290 (A. Ciallella); 0000-0001-5553-0066 (F. Hild)

joints is that, in the macroscopic response, they are associated with macroshear contributions to the strain energy to be used in the continuum model, and were proven to determine the overall response of the metamaterial (Spagnuolo et al., 2019; Spagnuolo, Andreaus, Misra, Giorgio and Hild, 2021; Spagnuolo, Yildizdag, Pinelli, Cazzani and Hild, 2022). It is worth noting that macroscale models used for describing pantographic sheets are based on second gradient 2D continua (Mindlin, 1965; Pideri and Seppecher, 1997; Luscher, McDowell and Bronkhorst, 2010; Turco, dell'Isola, Cazzani and Rizzi, 2016; Germain, 2020).

The specimen considered herein is called a pantographic block, namely, it consists of n pantographic sheets interconnected with hinges identical to those used inside each sheet. The design of the interconnecting hinges has been conducted in order to minimize any mechanical coupling phenomena inducing deformations of the pantographic block cross-sections (see Figure 1). Therefore, in the considered test, one may use 2D second gradient continua models accounting for the thickness of the block via a suitable increase of model stiffnesses. Special attention is to be devoted to the deformation mechanisms of such blocks when undergoing flexure. The study of deformations at the level of the mesostructure of the pantographic metamaterial is crucial. From the point of view of continuum models describing their mechanical response, the related flexural energy determines the part of macrostrain energy depending on the second gradient of macroplacement fields (Yang and Misra, 2012; Auffray, dell'Isola, Eremeyev, Madeo and Rosi, 2015; Placidi, Andreaus and Giorgio, 2017; Barchiesi, Eugster, Placidi and dell'Isola, 2019). The aim is then to observe experimentally the effects due to second gradient energy terms, in a mechanical test that reduces the strains relative to the elongation of the fibers (contributing to first gradient strain energy).

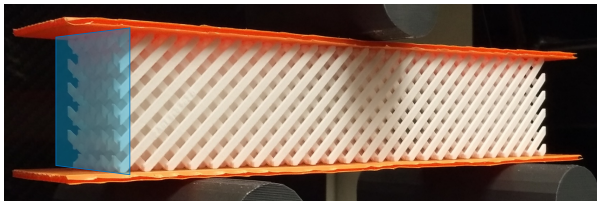

Figure 1: Example of pantographic block cross-section

In the present study, an *in situ* 3-point flexural test was monitored via X-ray tomography (Maire and Withers, 2014), and Digital Volume Correlation was utilized to measure displacement fields. As for Digital Image Correlation (Sutton, 2013), there are essentially two types of approaches to measure volumetric displacements, namely, local DVC in which small and independent subvolumes are registered (Bay, Smith, Fyhrie and Saad, 1999; Bay, 2008) and global (or FE-based) DVC (Roux, Hild, Viot and Bernard, 2008) for which the whole region of interest is meshed and correlated in a single analysis (Buljac, Jailin, Mendoza, Neggers, Taillandier-Thomas, Bouterf, Smaniotto, Hild and Roux, 2018). In the present case, FE-based DVC was utilized and a *unique* mesh was constructed for the whole metamaterial. FE-based DVC was already used to quantify the deformation of pantographic metamaterials subjected to torsion (Auger, Lavigne, Smaniotto, Spagnuolo, dell'Isola and Hild, 2021; Valmalle et al., 2022). However, to the authors' best knowledge, it was not yet applied to any flexural test on such metamaterials. Moreover, for the first time, the experimental evidence shown in the present work has made it possible to observe phenomena that one could only expect on a theoretical level. These phenomena were not previously observed; in fact, thanks to tomographic measurements and subsequent DVC analyses, it was possible to directly observe the deformations of the connecting hinges, which are normally hidden by the fibers. The observation of these deformations is crucial. In fact, it allows to validate the hypothesis that the pantographic block can be regarded as a superposition of pantographic sheets, which can be described by means of a 2D continuum model.

In fact, the models used in the description of this type of metamaterials involve terms that depend on second order gradient of the displacement field in the strain energy. For this reason, it is useful to have precise experimental information on such second gradient terms. These second gradient terms are only related to fiber bending. This is the reason why it is useful to isolate this deformation mechanism in order to obtain a study free from quantities linked to other deformation mechanisms. Typically, in a biased extension test (*i.e.*, biased with respect to the fiber directions, which are tilted by $\pm 45^{\circ}$ with respect to the horizontal direction) other types of deformation modes emerge. We refer, for example, to the elongation of fibers or the torsion of the connecting elements (hinges). Much greater energy contributions correspond to these mechanisms than to those of the bending of the fibers (typically, this is the same ratio as between extensional and flexural rigidities of a beam). It is therefore essential to devise methods to isolate the contribution of fiber bending. It was shown how to eliminate torsion contributions of hinges by replacing them with perfect pivots Spagnuolo (2020). In the present work, a 3-point flexural test was designed to eliminate, or minimize, the contributions of fiber elongation by only inducing fiber bending.

The outline of the paper is as follows. First, the *in situ* test is presented. Then, the different steps of FE-based DVC are introduced. The measured displacement fields, corresponding strain and gray level residual fields are analyzed to obtain quantitative information on the various deformation mechanisms at play in such test. Last, the modeling choices are described in which the assumption of nearly undeformable sections was probed.

2. In situ 3-point flexural test

The sample used herein, see Figures 1 and 2(a), was produced by selective laser sintering (SLS) from polyamide PA2200 powder and consisted in a rectangular cuboid of

size 203.5 × 43.5 × 33 mm. The beams had a rectangular cross-sectional area of 2.5 × 1.5 mm, and the connecting cylinders had a diameter of 0.90 mm with a length of 2 mm (Figure 2(b)). These values are nominal and were used to design the pantographic block in the CAD modeler. The resulting CAD file was then used to print the sample.

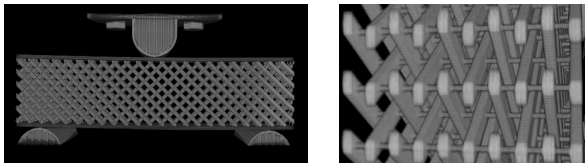

(a) (b)

Figure 2: (a) 3D rendering of the studied metamaterial (length: 203.5 mm, height: 43.5 mm) with a 100 µm / vx resolution. (b) Side view of hinges (0.90 mm in diameter) and beams

The 3-point flexural test was monitored using computed microtomography (Maire and Withers, 2014). Such imaging technique is non-intrusive and provides 3D images of samples tested *in situ* (Buffière, Maire, Adrien, Masse and Boller, 2010). Special 3D printed supports, made of ABS, were utilized (Figure 2(a)) to enable the total length and height of the sample to be imaged (*i.e.,* they had virtually the same X-ray absorption as the tested sample). Nylon screws were used to fix the supports to the aluminum alloy platens (Figure 3(a)). The load was applied by the longitudinal actuator moving the bottom platen of the *in situ* testing machine, which was controlled in position (with steps of 5 mm). The test was conducted up to the stroke limit (*i.e.,* 20 mm) of the machine. Cardboard was added to avoid friction and locking of the beam ends with respect to the supports (Figure 3).

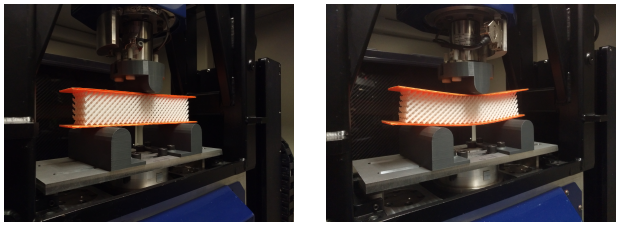

(a) (b)

Figure 3: (a) Sample in the reference configuration in the *in situ* testing machine. (b) Sample in the deformed configuration after the first loading step

Six tomographic scans were acquired, namely, two in the reference configuration for uncertainty quantification, and four in deformed configurations. The hardware parameters of the in situ setup are gathered in Table 1. Once cropped, the reconstructed volumes covered $50 \times 50 \times 100$ mm^3 with a 100 µm/vx resolution.

Series of 1,500 radiographs per scan were acquired to reconstruct 3D images of the deformed sample (Figure 4). This large number of radiographs per scan was needed since most of the sample occupied the whole length of the detector (Table 1). Overall, the quality of the reconstructed volumes was deemed very satisfactory for DVC calculations.

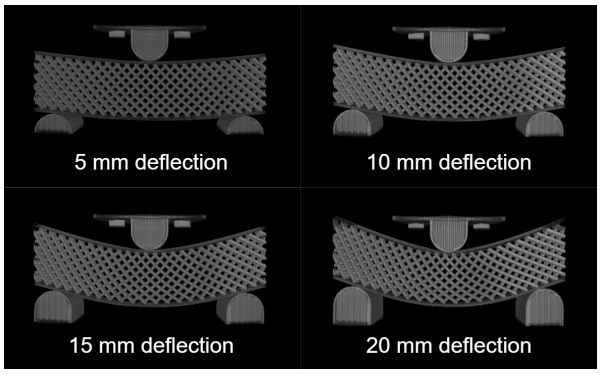

Figure 4: 3D renderings of the 4 deformed configurations

Figure 5 shows the plot of the reaction force versus prescribed displacement. This curve appears to be essentially linear. Four "discontinuity zones" are also observed, which correspond to the four tomographic acquisitions. They reflect small relaxations of the material that occurred as a result of test interruption and the effects of minute misalignment due to the rotation of the turntable.

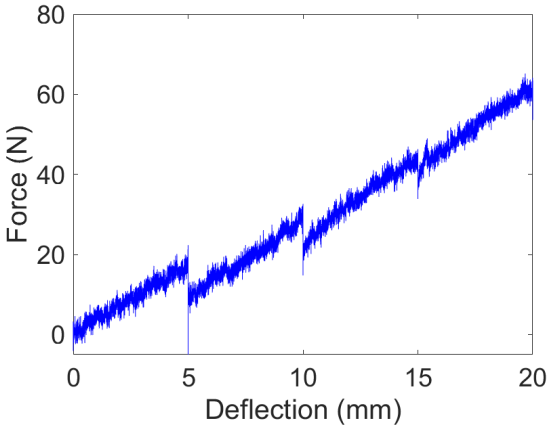

Figure 5: Force vs. deflection of the *in situ* 3-point flexural test

The reaction force plot is of crucial significance in this study. As briefly addressed in the introduction, pantographic metamaterials are describable as generalized (*i.e.,* second gradient) continua. In the latter ones, three contributions are introduced to the strain energy of the metamaterial, namely, one related to the elongation of the fibers, another one to the flexure of the fibers, and a third one (if any) to the torsion of the hinges. Specifically, for modeling the contribution related to flexure of the fibers, one has to introduce the second gradient of the placement field. This term is not present in theories based on classical Continuum Mechanics and, therefore, it is crucial to study it in order to fully characterize such metamaterials (Greco, Giorgio and Battista, 2017). In the present case, for the maximum prescribed displacement,

the energy contribution associated with the elongation of the fibers was expected to be negligible (Spagnuolo, 2020), while the contributions associated with fiber flexure and torsion of the hinges were present. The measured reaction force was therefore the combined signature of both deformation mechanisms. Since the measured reaction force was essentially linear with respect to the prescribed displacement, it was expected that nonlinear deformation mechanisms (*i.e.,* plasticity and damage) remained very limited. This point will be further discussed when local strain fields will be reported.

By comparing with theoretical results (Spagnuolo, 2020), it was observed that the measured reaction force was significantly higher than expected for this type of material. Two substantial differences are highlighted with respect to the investigated case:

i. in the present case, the metamaterial was not a single pantographic sheet, but consisted of a multilayered network, and therefore one must take into account the combined actions of various layers of bent fibers;

ii. the hinges were not perfect but deformed, and as widely discussed in the literature, most of the deformation energy of pantographic metamaterials is due to the deformation of hinges (Giorgio, 2016; Spagnuolo et al., 2019).

3. Different DVC steps

In the following analyses, two different scales were considered. Macroscale DVC dealt with a mesh for which all the morphological details of the metamaterial were not accounted for. It was useful to initialize mesoscale analyses (in which the actual architecture of the metamaterial was meshed) given the large displacement amplitudes between each acquisition (Figure 4). The macroscale measurements were subsequently compared to model predictions at the same scale. The mesoscale enabled deformation mechanisms to be quantified for the hinges. Various DVC steps had thus to be tailored to the present case.

3.1. Mesh in the reference configuration

FE-based DVC (Roux et al., 2008; Hild, Bouterf, Chamoin, Mathieu, Neggers, Pled, Tomičević and Roux, 2016) was used in the present analyses. Such approach requires an FE mesh to be constructed. In the present case, the starting point was the STL model of the to-be-printed pantographic block. This initial information corresponded to the nominal configuration of the digital twins (Figure 6). A 3D mesh made of 4-noded (T4) tetrahedra was constructed from the STL model with the PDE toolbox of Matlab. Once generated, the mesh was cropped in order to measure displacement fields only between the two outer supports, and for the mesh to remain within the monitored volume when deformed. The voxelized twin, which was needed for DVC purposes, was a mask in which each voxel lying within the mesh was assigned a nonzero value. It was also constructed from the STL model of the nominal configuration (Figure 6). The STL model was cropped (with Avizo Fire 8.0) to be consistent with the DVC ROI, and to coincide with the size of the used mesh. With this cropped STL file, a ray tracing algorithm (Patil and Ravi, 2005) was used to create the voxelized twin.

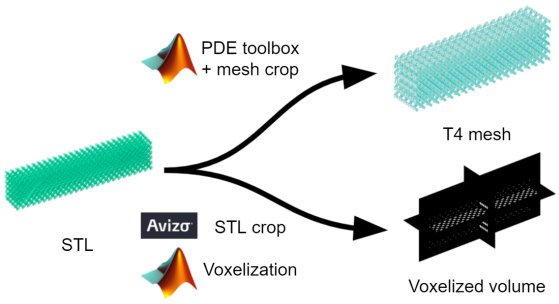

Figure 6: Digital twins of the nominal configuration of the studied metamaterial

Figure 7 shows the mesh in the nominal configuration. The mesh initially contained 62,270 nodes and 177,067 T4 elements whose mean size (measured as the cube root of the average elementary volume) was 6 vx. Another issue appeared, namely, the PDE mesher generated few very small elements (with volumes of the order of one voxel) that would have resulted in a very poor conditioning of the Hessian matrices used in DVC calculations. The choice was made to remove the elements whose size was less than 2 vx. This slightly modified mesh contained 62,261 nodes and 171,755 T4 elements whose mean length still was 6 vx. All hinges were explicitly meshed. Conversely, the geometric details of each beam close to the connections were not as fine (Figure 7(b-d)). This choice resulted from compromises between mesh fineness, voxel resolution and size of the DVC (Hessian) matrix.

Because of small errors due to printing, mispositioning of the sample and the application of a preload, the experimental reference configuration did not coincide with that of the digital twin. Therefore, a backtracking procedure (Auger et al., 2021) was needed to fit the mesh constructed with the digital twin onto the printed configuration. Another route could have been to resort to so-called shape correlation (Kleinendorst, Hoefnagels and Geers, 2019). However, in the present case, standard DVC was sufficient with no need for mechanical regularization. The procedure consisted in registering the printed configuration with the voxelized digital twin (Figure 6). An auxiliary mesh encompassing the volume in the printed configuration was considered and DVC was run. It is worth noting that this mesh was also used in the DVC analyses at the macroscale.

Figure 9 shows the displacement field that had to be applied between the printed and nominal configurations. The rigid body translations were taken out since they were due to the fact that the reconstruction frame and that of the digital twin did not coincide. The displacement fields along the vertical and longitudinal directions were consistent with a flexural preload that was applied. The displacement

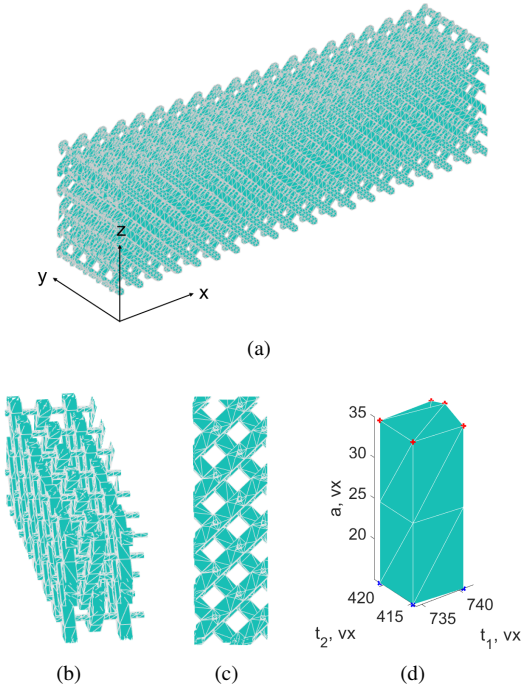

Figure 7: (a) Mesoscale mesh of the nominal configuration with its reference frame. Side (b) and front (c) views of hinges. (d) Detail of one individual hinge ans its reference frame (axial and tangential directions). The red and blue nodes depict the top respectively the bottom planes used to measure displacement and rotation jumps

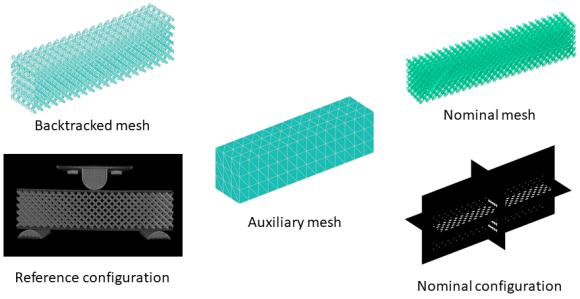

Figure 8: Reference (printed) configuration to be registered with the nominal configuration via DVC using an auxiliary (*i.e.*, macroscopic) mesh encompassing the reference configuration. The nominal mesh is then backtracked

field along the transverse direction also had the signature of flexural preload but with smaller amplitude.

3.2. Uncertainty quantification

The reconstructed volumes were registered using the Correli 3.0 framework (Leclerc, Neggers, Mathieu, Hild and Roux, 2015) in which Hencky regularization (dell'Isola, Seppecher, Spagnuolo, Barchiesi, Hild, Lekszycki, Giorgio, Placidi, Andreaus, Cuomo, Eugster, Pfaff, Hoschke, Langkemper, Turco, Sarikaya, Misra, De Angelo, D'Annibale, Bouterf, Pinelli, Misra, Desmorat, Pawlikowski, Dupuy, Scerrato, Peyre, Laudato, Manzari, Göransson, Hesch, Hesch,

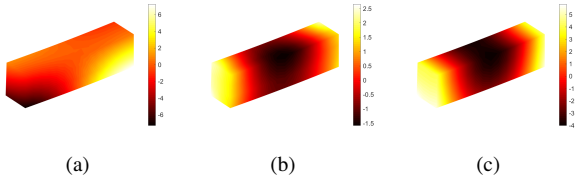

Figure 9: Displacement fields in the x (*i.e.*, longitudinal) (a), y (*i.e.*, transverse) (b) and z (*i.e.*, vertical) (c) directions obtained by the backtracking procedure. The fields are shown on the deformed configuration and expressed in voxels (1 vx ≡ 0.1 mm)

Franciosi, Dirrenberger, Maurin, Vangelatos, Grigoropoulos, Melissinaki, Farsari, Muller, Abali, Liebold, Ganzosch, Harrison, Drobnicki, Igumnov, Alzahrani and Hayat, 2019b) was implemented for the mesoscale analyses (Tab. 2), since virtually no contrast existed within the printed parts (except few porosities), which prevented analyses to be performed at even lower scales. In the present case, the measured displacement field $\mathbf{u}$ was parameterized with the nodal displacements associated with the finite element discretization based on 4-noded (T4) tetrahedra (Hild et al., 2016).

At this stage, the regularization length was not yet selected. Therefore, the uncertainties were studied for different regularization lengths ℓ_m with the same mesh. The noise floor levels were assessed using the two scans of the reference configuration. DVC analyses were run with the backtracked mesh (Figures 8). Rigid body motions were subtracted from the measured displacement fields, the standard deviations of each nodal displacement component was estimated and are displayed in Figure 10(a). The measurement uncertainties were very close for the three spatial directions for a given regularization length. The (classical) compromise between measurement uncertainty and regularization length was found (Leclerc, Périé, Hild and Roux, 2012). However, it was observed that the uncertainty level was not solely controlled by acquisition noise since the power $-3/2$ dependence of the displacement uncertainty was not followed. This result proves that other sources of error also occurred, which was expected when dealing with tomographic acquisitions (Buljac et al., 2018). For large regularization lengths, standard displacement uncertainties as low as 10^{-2} vx were reached thanks to the regularization strategy used herein.

The maximum principal strain ϵ_1 and the von Mises equivalent strain ϵ_{vM} will be reported in the sequel. The latter one was considered to assess the level of plastic strains in the hinges and beams. Their standard uncertainties were therefore evaluated as well. They correspond, for each strain descriptor, to the standard deviation of the elementary quantities assessed in the whole mesoscale mesh. The larger the regularization length, the lower the standard strain uncertainties (Figure 10(b)). Apart from the second principal strain (ϵ_2), all three strain components (ϵ_1, ϵ_3 and ϵ_{vM}) had virtually identical uncertainties. When large regularization

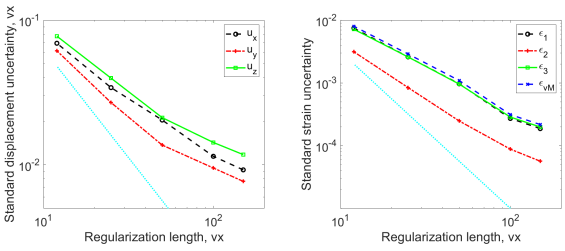

(a) (b)

Figure 10: Standard displacement (a) and strain (b) uncertainties as functions of the regularization length ℓ_m. The physical size of one voxel is 0.1 mm. The cyan dotted lines show power law interpolations with exponents $-3/2$ (a) and $-5/2$ (b)

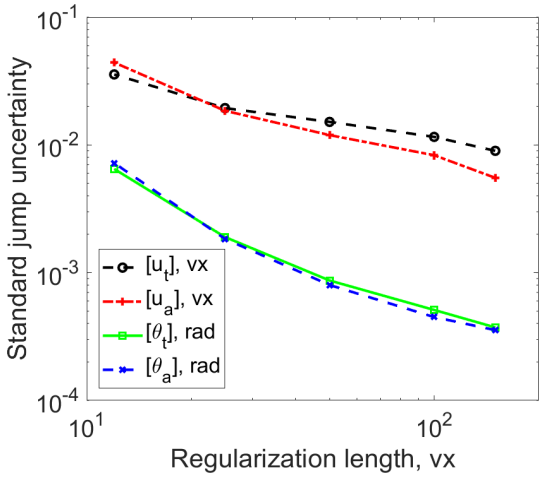

Figure 11: Standard displacement (a) and rotation (b) jump uncertainties as functions of the regularization length ℓ_m. The physical size of one voxel is 0.1 mm

lengths were selected, the strain uncertainties were compatible with the measurement of elastic strains. Conversely, when less regularized, DVC analyses will not allow elastic strains to be measured accurately. Conversely, plastic strains could be quantified even for very small regularization lengths (for levels greater than 10^{-2}). Last, let us note that the power law interpolation with an exponent of $-5/2$ was not followed for the same reasons as those discussed for the displacement uncertainties.

Last, the uncertainties were evaluated for the 1,935 hinges that were explicitly meshed (Figure 7(b-d)). The axial direction of the hinges corresponded to the y-direction in the nominal configuration. There are two nodal planes connecting each hinge to the beams (*i.e.,* bottom and top sections). For each of them, the mean displacements and rotations were computed. The displacement jumps were obtained by subtracting the mean displacement of the bottom section of the hinge to that of the top section (Figure 7(d)). Similarly, the rotation jumps were assessed by subtracting the mean rotation of the bottom section to that of the top section. In the following, the axial components of the rotation ($[\![\theta_a]\!]$) and displacement ($[\![u_a]\!]$) jumps were computed in addition to the corresponding transverse components (*i.e.,* the norm of the two components in the plane normal to the axial direction). Figure 11 shows their standard uncertainty levels as functions of the regularization length ℓ_m. For the displacement jumps, the uncertainties were lower than those of the nodal displacements (Figure 10(a)). For the rotation jumps, the corresponding uncertainties were very close to those of the minor and major principal strains (Figure 10(b)).

3.3. Initialization

Due to the large deformations between consecutive scans (Figure 4), the DVC calculations had to be initialized. A digital image correlation (DIC) algorithm was used on each nodal cross-section of the macromesh encompassing the sample (*i.e.,* the auxiliary mesh of the backtracking procedure, see Figure 8) seeking in-plane rigid body motions (*i.e.,* assuming that there was no out-of-plane motion. Because the top grip was motionless in this experiment, the middle section of the pantograph was expected to be essentially motionless. Accordingly, the DIC calculations were run from the middle plane along the right and the left directions separately, using the rigid body of the previous nodal plane to initialize the next DIC calculation.

The displacement field found at this stage was then used as initialization for incremental DVC calculations (Figures 12 and 13), which converged in less than 10 iterations for a criterion on the L2-norm of the displacement corrections that was less than 10^{-2} vx. The displacements along the (vertical) z-direction near the outer supports (corresponding to the loading) had very large amplitudes between each scan (about 50 vx). The incremental calculations converged easily because such large displacements were initialized thanks to the DIC procedure.

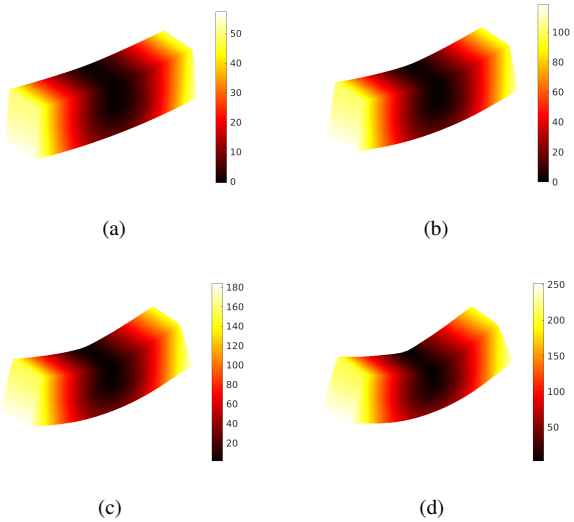

(a) (b) (c) (d)

Figure 12: Initialization results in terms of displacements (expressed in voxels, 1 vx ≡ 0.1 mm) along the z (*i.e.,* vertical) direction for the different deformed configurations. (a) 5 mm, (b) 10 mm, (c) 15 mm and (d) 20 mm deflections

The deformed configurations show that rather large displacements occurred in the (longitudinal) x-direction (Figure 13) as well. They were induced by large rotations that took place in the vicinity of the outer supports. Such displacements were not pre-corrected by the initialization procedure, contrary to those in the z-direction.

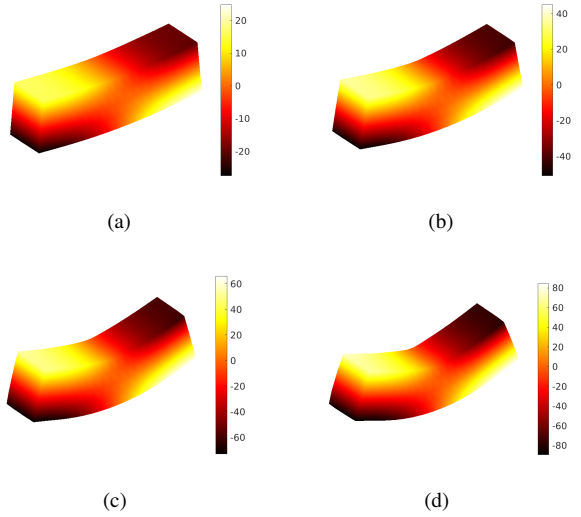

Figure 13: Initialization results in terms of displacements (expressed in voxels, 1 vx ≡ 100 µm) along the x (*i.e.,* longitudinal) direction for the different deformed configurations. (a) 5 mm, (b) 10 mm, (c) 15 mm and (d) 20 mm deflections

3.4. Direct DVC calculations

The displacement fields measured on the macroscopic mesh (Figures 12 and 13) were used to initialize DVC analyses at the mesoscale. They were run directly for the 4 deformed scans using the backtracked mesh (Figure 8). The DVC calculations were stopped when the L2-norm of displacement corrections were less than 10^{-2} vx. All calculations converged quickly. Had the DVC analyses not been initialized, the convergence would have been very slow, if possible.

Since regularized DVC was selected at the mesoscale, the measured displacement field $\mathbf{u}$ was determined by minimizing the sum of squared gray level differences

$$\Phi_c^2(\{\boldsymbol{v}\}) = \frac{1}{|\mathrm{ROI}|}\sum_{\mathrm{ROI}}\left(I_0(\mathbf{x}) - I_t(\mathbf{x}+\mathbf{u}(\mathbf{x},\{\boldsymbol{v}\}))\right)^2 \quad (1)$$

where the gray level residual φ_c at each voxel $\mathbf{x}$ reads

$$\varphi_c = I_0(\mathbf{x}) - I_t(\mathbf{x}+\mathbf{u}(\mathbf{x})) \quad (2)$$

penalized by the equilibrium gap

$$\Phi_m^2(\{\boldsymbol{v}\}) = \{\boldsymbol{v}\}^\top[\mathbf{K}]^\top[\mathbf{K}]\{\boldsymbol{v}\} \quad (3)$$

such that

$$\{\boldsymbol{v}\}_{\mathrm{meas}} = \arg\min_{\{\boldsymbol{v}\}}\left(\Phi_c^2(\{\boldsymbol{v}\}) + w_m\Phi_m^2(\{\partial\boldsymbol{v}\})\right) \quad (4)$$

where $\{\partial\boldsymbol{v}\}$ denotes the column vector of incremental nodal displacements from one analysis to the next, $[\mathbf{K}]$ the rectangular stiffness matrix associated with bulk and free surface nodes, I_0 the volume in the reference configuration, I_t the volume in the deformed configuration, and ROI the selected region of interest. The regularization weight w_m is proportional to the regularization length ℓ_m raised to the power 4 (Taillandier-Thomas, Roux, Morgeneyer and Hild, 2014). It is worth mentioning that since regularization was performed at the mesoscale, the stiffness matrix is associated with a standard (*i.e.,* Cauchy) continuum formulation.

Figure 14(a) shows the change of the root mean square (RMS) gray level residual Φ_c as a function of the equilibrium gap Φ_m for five different regularization lengths. In addition to the four acquisitions under different deflections, a fifth result was added, which corresponds to that of the uncertainty quantification for which a second scan was acquired in the reference configuration. This first case always led to the lowest gray level residuals. The fact that the gray level residuals remained rather close to these minimum levels when the sample was deformed is an indication that the registrations were successful. When the regularization length was increased, the equilibrium gap Φ_m decreased as more weight was put on the penalty term. Conversely, the gray level residuals increased as the sample was more deformed for large regularization lengths. This trend indicates that the regularization was too strong for the largest regularization lengths (*i.e.,* Hencky elasticity was no longer sufficient to globally account for the underlying behavior).

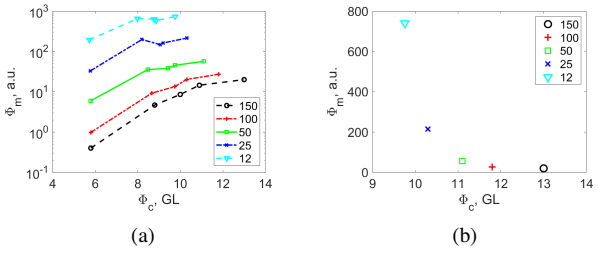

Figure 14: (a) Equilibrium gap Φ_m vs. gray level residual Φ_c for the five analyzed scans and for different regularization lengths (expressed in voxels, 1 vx ≡ 0.1 mm). (b) Corresponding plot for the last deformation step. The digitization of the registered volumes was 8 bits

One of the criteria used to select the regularization weight consists in looking for the maximum curvature (*i.e.,* L-curve criterion (Hansen, 2000)) in the previous plot for a given deformation step (*e.g.,* for the maximum deflection, see Figure 14(b)). According to that criterion, the regularization length $\ell_m = 25$ vx provided the best balance between Φ_c and Φ_m. This result applied to all the considered deflections and $\ell_m = 25$ vx was therefore selected (Table 2).

Figure 15 shows the gray level residual fields at the end of direct calculations for each loading step. The gray levels were the lowest close to the middle section for each scan as

it did not move much (because the middle support was motionless). Higher levels were observed at the two ends of the pantograph because of very large displacements (Figures 16 and 17) making the calculations more difficult. The top and bottom surface of the pantograph also concentrated higher residual levels as there was corrugated cardboard (undulating polypropylene sheet commonly known as coroplast) on the top and bottom parts of the sample to ensure smooth contact between the pantograph and the supports. Overall, the residuals remained sufficiently low for the DVC results to be deemed trustworthy.

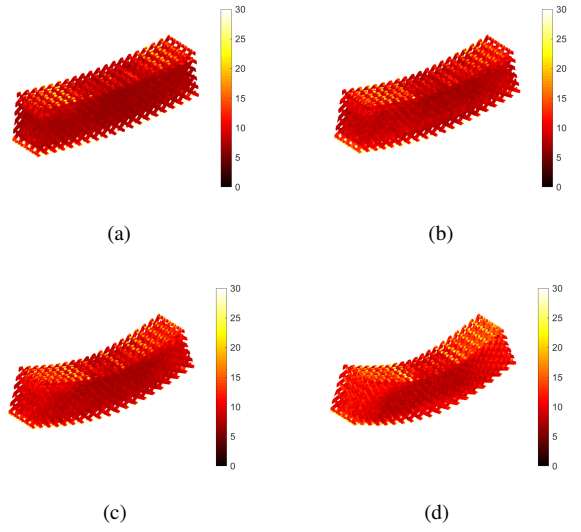

Figure 15: Gray level residuals for the different deformed configurations. (a) 5 mm, (b) 10 mm, (c) 15 mm and (d) 20 mm deflections. The digitization of the registered volumes was 8 bits

4. Analysis of the results

4.1. Displacement fields

Figure 16 shows the measured vertical displacement fields on the corresponding deformed configurations. Their overall levels were similar to those measured at the macroscale (Figure 12). This observation shows that the macroscale analysis provided good initial guesses for the global characterization of the kinematics of the flexural test.

Figure 17 displays the measured longitudinal displacement fields on the corresponding deformed configurations. The displacements essentially characterize the section rotations (as was already observed on the macroscale analyses, see Figure 13), and their amplitudes increased linearly with the deflection. Very large levels were observed, which could be captured thanks to the various initialization steps that were followed herein.

In Figure 18, the measured displacement fields along the transverse direction are shown for the four deflections. Their amplitudes were significantly lower than those observed for the other two displacement components (Figure 16 and 17).

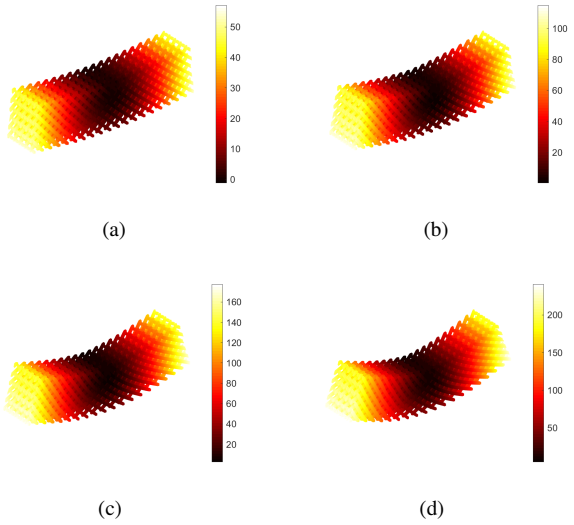

Figure 16: Displacement fields along the z (*i.e.*, vertical) direction for the different deformed configurations. (a) 5 mm, (b) 10 mm, (c) 15 mm and (d) 20 mm deflections. The displacements are expressed in voxels (1 vx $\equiv$ 0.1 mm)

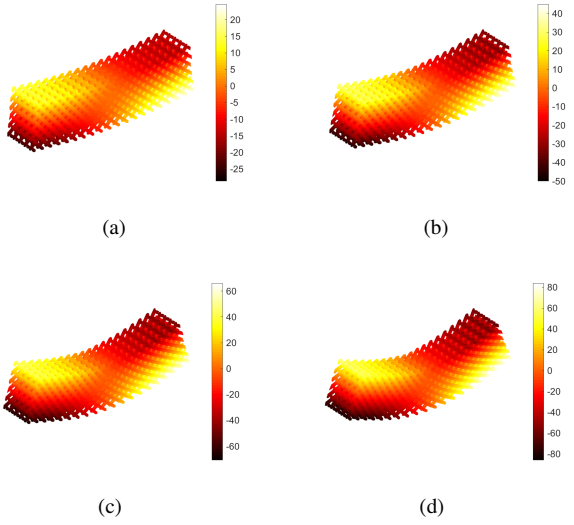

Figure 17: Displacement fields along the x (*i.e.*, longitudinal) direction for the different deformed configurations. (a) 5 mm, (b) 10 mm, (c) 15 mm and (d) 20 mm deflections. The displacements are expressed in voxels (1 vx $\equiv$ 0.1 mm)

In some 3-point flexural tests (Maati, Tabourot, Balland and Belaid, 2020), the emergence of Poisson effects in one direction perpendicular to that of the prescribed displacement were observed. This effect, which generally occurs in bias-extension or bias-compression tests on pantographic metamaterials as studied in this work was not detected experimentally or was almost absent, as shown in Figures 16-18. As pointed out previously, a major role in the mechanics of pantographic metamaterials was played by the hinges connecting the fiber layers. The emergence of the

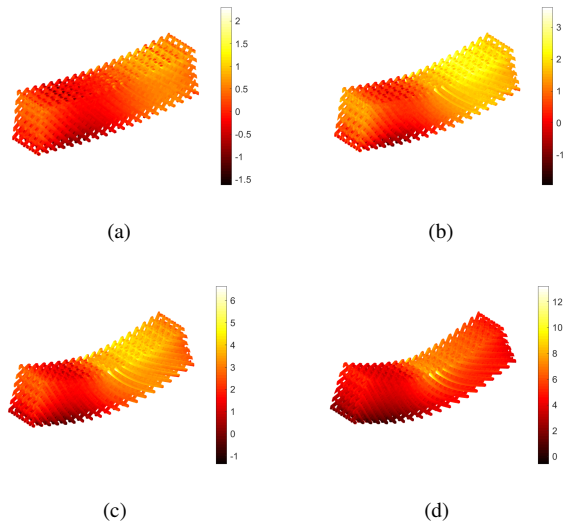

Figure 18: Displacement fields along the y (*i.e.*, transverse) direction for the different deformed configurations. (a) 5 mm, (b) 10 mm, (c) 15 mm and (d) 20 mm deflections. The displacements are expressed in voxels (1 vx $\equiv$ 0.1 mm)

Poisson's effect is related to the aspect ratio of the cylinders constituting the hinges. With slender hinges, as in the present case, this effect was hindered. Instead, such effect would be observed with hinges with a low aspect ratio. Further investigations are needed to clarify these questions.

4.2. Strain fields

Von Mises and maximum principal strain fields are shown in Figure 19. Both fields were equivalent in overall distributions. There was one remarkable phenomenon that was the opposite behavior of the two mutually orthogonal families of beams. Near the outer supports, the family of beams that was oriented toward the middle of the pantograph concentrated most of the strains (and thus most of the stresses). This observation is unusual for a standard flexural test to have the highest strain levels near the outer supports and not around the mid-section. Since the equivalent von Mises strain was greater than 1% in some areas at the end of the test, it was concluded that inelasticity had occurred even though the load/displacement response was still linear (Figure 5). This conclusion was confirmed by the fact that when large regularization lengths were considered, higher RMS gray level residuals were observed (Figure 14).

To further investigate this phenomenon, the maximum principal strain field is shown separately for the two families of beams in Figure 20. Apart from the first loading step, the strain distribution was no longer symmetric with respect to the mid-section plane. The deformation concentrated in the beams oriented toward the central section and located at both ends of the metamaterial.

4.3. Hinge kinematics

The analysis now focuses on the 1,935 hinges. The first set of results is related to the deformation mechanism

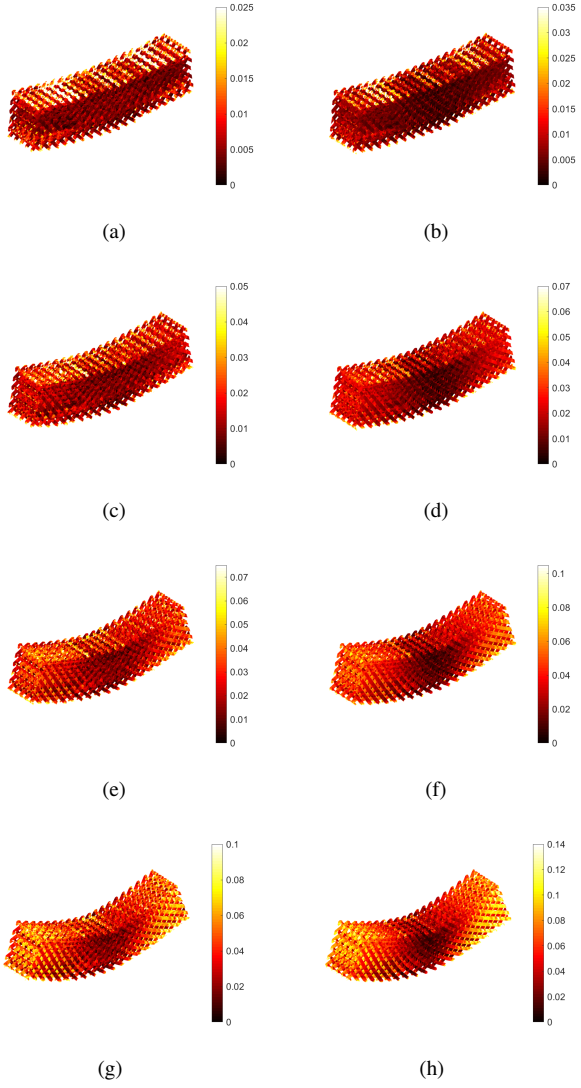

Figure 19: Von Mises equivalent strain (left) and maximum principal strain (right) fields for the 4 different deformed configurations. (a,b) 5 mm, (c,d) 10 mm, (e,f) 15 mm and (g,h) 20 mm deflections

that occurs in flexure of such metamaterials. The Gaussian curvature of a surface at a given point is the product of the principal curvatures κ_1 and κ_2. Monoclastic surfaces are characterized by flexure occurring in only one direction (*i.e.*, zero Gaussian curvature). Synclastic surfaces have principal curvatures with the same sign (*i.e.*, positive Gaussian curvature). Conversely, anticlastic surfaces have principal curvatures with opposite signs (*i.e.*, negative Gaussian curvature). In the present case, the deformed (upper) surface defined by the center of gravity (x, y) of each hinge was analyzed when computing $u_z(x, y)$ once the rigid body motions were subtracted. Figure 21 shows the corresponding maps for the four deflection steps. The overall shape remained the same; only the amplitude increased with the applied displacement of the supports.

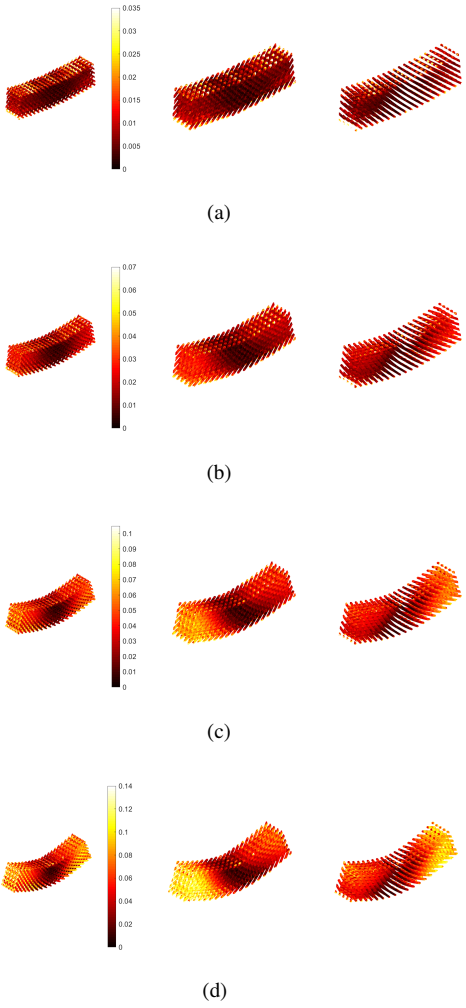

Figure 20: Maximum principal strain fields shown for the 4 different deformed configurations on the whole mesh (left), first family of beams (center) and second family of beams (right). (a) 5 mm, (b) 10 mm, (c) 15 mm and (d) 20 mm deflections

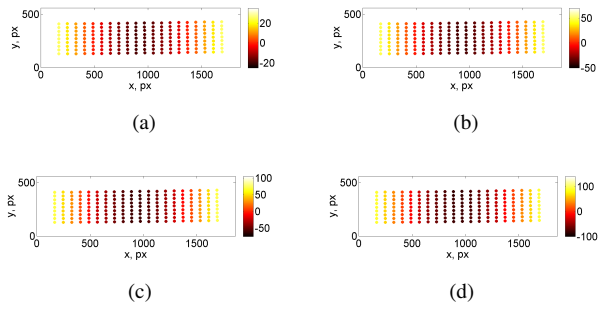

Figure 21: Vertical displacement fields u_z of each hinge center of gravity (of the upper row of the pantographic block) once the rigid body motions were subtracted. (a) 5 mm, (b) 10 mm, (c) 15 mm and (d) 20 mm deflections. The displacements are expressed in voxels (1 vx $\equiv$ 0.1 mm)

From the previous results, it was easy to conclude directly on the deformation mode of the studied surface since it was fully dominated by the flexural mode in the longitudinal direction. Consequently, a parabolic fit was performed and the curvatures were assessed at the center of the considered surface (Figure 22). The major principal curvature was linearly related to the prescribed deflection. This is the signature of a flexural test. The minor curvature amplitude was significantly lower than that of the major curvature (as expected from Figure 21). Yet, it was negative, which indicated that the deformation mode was slightly anticlastic (*i.e.,* negative Gaussian curvature). Interestingly, for the largest deflection step, the Gaussian curvature decreased significantly, which further indicated that nonlinear effects may have occurred.

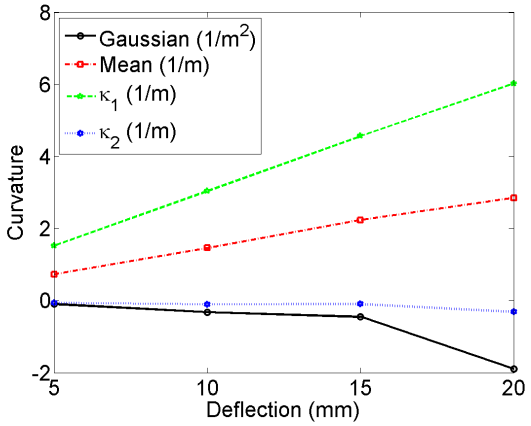

Figure 22: Principal curvatures κ_1 and κ_2, corresponding mean and Gaussian curvatures for the center of the upper surface of the pantographic block (Figure 21)

The second set of results is related to the displacement and rotation jumps for each hinge. As in the uncertainty quantification (Figure 11), the axial and transverse components of the rotation and displacement jumps are reported. Let us note that the amplitudes were at least one order of magnitude higher than their standard uncertainties. Consequently, their levels were deemed trustworthy. Figure 23(a) shows the axial displacement jump for each hinge for the last loading step. The hinges in the central part of the sample underwent rather modest displacement jumps (*i.e.,* less than 0.5 vx in absolute value). Conversely, higher absolute levels were observed closer to the external supports.

The tangential displacement jumps were higher in the central part of the sample in comparison to their levels closer to the external supports (Figure23(b)). Similar trends were observed for the axial rotation jumps (Figure23(c)). However, their sign was alternating from one layer to the next. This was due to the fact that the two families of beams did not deform in a similar way (Figure 20). For the transverse rotation jumps (Figure23(d)), they were also alternating from one layer to the next. Their amplitudes remained smaller than those of the axial rotation jumps.

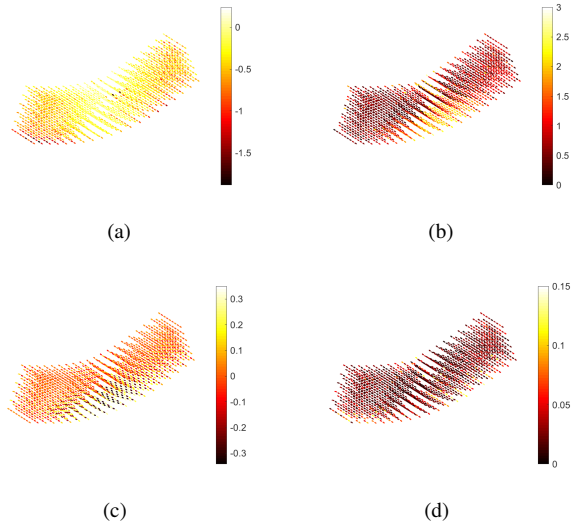

Figure 23: Axial (a) and transverse (b) displacement jumps (expressed in voxels, 1 vx ≡ 0.1 mm) for each hinge. Corresponding axial (c) and transverse (d) rotation jumps (expressed in rad) for each hinge. The results are shown for the last deformed configuration

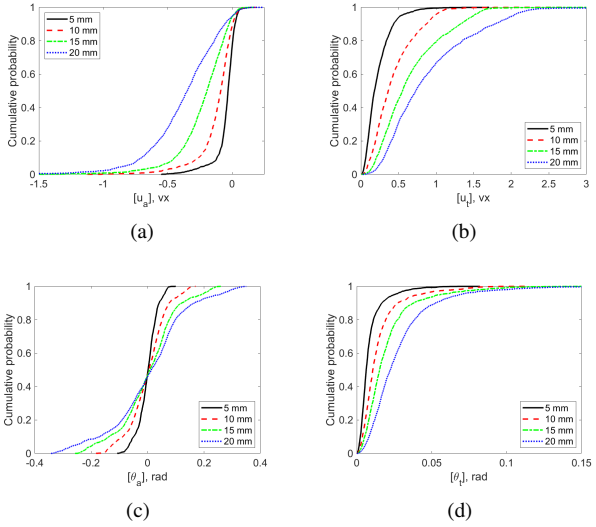

Figure 24: Cumulative plots of axial (a) and transverse (b) displacement jumps for the four applied deflections. The displacements are expressed in voxels (1 vx ≡ 0.1 mm). Corresponding plots for the axial (c) and transverse (d) rotation jumps

The distribution of the four previous quantities are displayed in Figure 24 in terms of cumulative plots for the four deformation steps. For all four jumps, the larger the deflection, the wider their distributions. For the axial displacement jumps (Figure 24(a)), they were mostly negative (*i.e.,* shortening of the hinges). The amplitude of the transverse displacement jumps (Figure 24(b)) was significantly higher than that in the axial direction for all deflections. The distribution of axial rotation jumps (Figure 24(c)) was virtually symmetric with respect to the 0 rad angle, which was due to the different deformation of the two families of beams (Figure 20). The amplitudes of the transverse rotation jumps (Figure 24(d)) were lower than those of the axial rotation jumps for any loading step. These observations show that the two dominant deformation modes of the hinges were shear and torsion. Conversely, axial contraction and flexure remained less active.

Very similar results were obtained on the lower row of hinges. For the sake of conciseness, they are not further discussed. Last, given the fact that the transverse displacements remained very small (Figure 18) in comparison to their vertical and horizontal components (Figures 16 and 17), the two lateral surfaces of the pantographic block did not experience significant deformations.

5. Prediction of deformation patterns in 3-point flexure of pantographic blocks with elastic hinges

5.1. Modeling overview

The design of pantographic sheets involved two mutually orthogonal fiber arrays that were mechanically interacting thanks to continuously distributed and equidistant cylindrical joints. Their mechanical and geometric properties greatly influence the overall response of pantographic sheets. When these joints are very stiff the resulting behavior after homogenization is governed by an orthotropic first gradient strain energy (Boutin et al., 2017). Conversely, when they have small torsional rigidity, suitably rescaled with respect to the inter-joint distance, the response corresponds to that of a second gradient medium (dell'Isola, Seppecher, Alibert, Lekszycki, Grygoruk, Pawlikowski, Steigmann, Giorgio, Andreaus, Turco, Gołaszewski et al., 2019a; dell'Isola et al., 2019b). Elastic joints induce a microdeformation mechanism that allows for relative rotations of the fibers. In the limit case when they behave as perfect hinges, the flexural energy of the pantographic architecture becomes dominant and at the macroscale second gradient effects are observed.

Assuming that the cylindrical hinges were small and stiff enough, the two families of fibers can be described in terms of the same macrodisplacement field, as the hinges exert elastic or any constraint on their relative rotations. In macroscopic descriptions, the joints control the shear deformations and their torsional energy is equal to the macroshear energy. It was proven that small variations of their mechanical and geometric properties caused large changes in macromechanical properties, including a transition from first to second gradient macrostrain energies (Cuomo, dell'Isola,

Greco and Rizzi, 2017). Therefore, the models to be used in the description of pantographic sheets must be associated with second gradient 2D continua (dell'Isola et al., 2016).

5.2. Pantographic blocks

The mechanical properties of the interconnecting hinges were designed to reduce all mechanical couplings that may cause deformations of cross-sections of the pantographic block. This choice was made in order to allow for the use of already available 2D second gradient continuum models. The three-dimensionality of the block was simply accounted for by using a suitable increase of 2D pantographic sheet stiffnesses (*i.e.,* strain energy multiplied by the number of pantographic sheets composing the block).

In 3-point flexure, as shown above, fiber flexure became dominant at the mesolevel. As a consequence, in the macroscopic mechanical response, the second gradient strain energy dominates. The only surviving first gradient energies are those relative to shear deformations, which are tuned by suitably choosing the geometric properties of cylindrical hinges (Spagnuolo et al., 2019; Giorgio, 2016).

5.3. Pantographic sheet model

In the previous section, it was observed that, notwithstanding the fact that a 3D pantographic block was studied, a 2D model may be adopted because all deformations were essentially planar. The fact that multiple pantographic sheets were printed will be taken into account by suitably correcting the constitutive parameters. Let us consider a reference configuration of a pantographic lattice (Figure 25). A 2D second gradient continuum model for properly describing the pantographic sheet was introduced by dell'Isola et al. (dell'Isola et al., 2016) and generalized by Spagnuolo et al. (Spagnuolo, Barcz, Pfaff, dell'Isola and Franciosi, 2017). In the following, the original model (dell'Isola et al., 2016) was selected for the sake of simplicity. Let $(\mathbf{D}_1, \mathbf{D}_2)$ be an orthogonal basis for the reference configuration, where both vectors are aligned with the fiber directions (*i.e.,* orthogonal in the reference configuration).

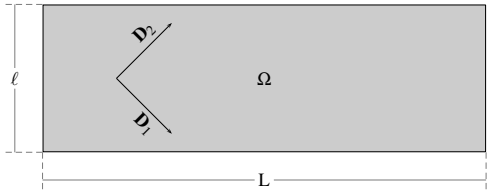

Figure 25: Reference configuration of a pantographic block

A 2D continuum is considered whose reference shape is given by a rectangular domain $\Omega = [0, \mathrm{L}] \times [0, \ell] \subset \mathbb{R}^2$, where L and ℓ are identified as the lengths of the sides of the continuum medium (Figure 25) and $\mathrm{L} = 3\ell$. The current shape of the rectangle is mathematically described by a regular placement function $\boldsymbol{\chi} : \Omega \to \mathbb{R}^2$. In Ref. (dell'Isola et al., 2016), it was shown how, by means of asymptotic homogenization (dell'Isola et al., 2016) and assuming that $\boldsymbol{\chi}(\cdot)$ is at least twice differentiable, the macroscopic strain energy for the pantographic metamaterial is obtained

$$\begin{aligned}\mathcal{U}(\boldsymbol{\chi}(\cdot)) &= \int_\Omega \sum_\alpha \frac{K_e}{2}(||\boldsymbol{F}\mathbf{D}_\alpha|| - 1)^2 \, d\Omega \\ &+ \int_\Omega \sum_\alpha \frac{K_b}{2}\left[\frac{\boldsymbol{\nabla F}|\mathbf{D}_\alpha \otimes \mathbf{D}_\alpha \cdot \boldsymbol{\nabla F}|\mathbf{D}_\alpha \otimes \mathbf{D}_\alpha}{||\boldsymbol{F}\mathbf{D}_\alpha||^2}\right. \\ &- \left.\left(\frac{\boldsymbol{F}\mathbf{D}_\alpha}{||\boldsymbol{F}\mathbf{D}_\alpha||} \cdot \frac{\boldsymbol{\nabla F}|\mathbf{D}_\alpha \otimes \mathbf{D}_\alpha}{||\boldsymbol{F}\mathbf{D}_\alpha||}\right)^2\right] d\Omega \quad (5)\end{aligned}$$

where $\boldsymbol{F}$ denotes the deformation gradient $\boldsymbol{\nabla}\boldsymbol{\chi}$, and $\left(\boldsymbol{\nabla F}|\mathbf{D}_\alpha \otimes \mathbf{D}_\alpha\right)^\beta = F^\beta_{\alpha,\alpha} = \chi^\beta_{,\alpha\alpha}$, with $\alpha, \beta = \{1, 2\}$. The parameters K_e and K_b represent, respectively, the elongation and bending stiffnesses. The first integral in Equation (5) is related to fiber elongation while the second one refers to fiber flexure. It is worth noting that the flexural energy is written in terms of the gradient of the deformation tensor $\boldsymbol{\nabla F}$, which corresponds to the second gradient of the placement function $\boldsymbol{\nabla}^2\boldsymbol{\chi}$. This observation is consistent with the fact that the second gradient term is representative of fiber flexure.

If microstructural joints cannot be considered as perfect hinges, as in the present study, one has to deal with their deformation adding further terms to the strain energy (Equation (5)). The hinges are modeled as elastic cylinders. Consequently, one should take into account their torsion and shear deformations. These two deformation mechanisms are sometimes negligible. In the present case, the diameter of the pivots was 0.90 mm and their height 2 mm. They were considered slender and their microshear should be taken into account. Yet, the experiment was designed to minimize all deformations except fiber flexure. For this reason, microshear was neglected.

A simple form for the microtorsion (corresponding to macroshear) energy term was assumed to depend on the angle between the interconnected fibers from the pivot raised to the power γ (dell'Isola et al., 2016). The latter may be obtained from the fit of experimental data, and may depend on the type of material with which the pantographic structure was additively manufactured. The proposed form for the shear energy reads

$$\begin{aligned}&\mathfrak{U}_s(\boldsymbol{\chi}(\cdot))= \\ &=\int_\Omega \frac{K_s}{2}\left|\cos^{-1}\left(\frac{\boldsymbol{F}\mathbf{D}_1}{||\boldsymbol{F}\mathbf{D}_1||} \cdot \frac{\boldsymbol{F}\mathbf{D}_2}{||\boldsymbol{F}\mathbf{D}_2||}\right) - \frac{\pi}{2}\right|^\gamma d\Omega \quad (6)\end{aligned}$$

where K_s is the macro-shear stiffness, which is related to the torsional stiffness of the cylinders modeling the connecting joints. The term $\cos^{-1}\left(\frac{\boldsymbol{F}\mathbf{D}_1}{||\boldsymbol{F}\mathbf{D}_1||} \cdot \frac{\boldsymbol{F}\mathbf{D}_2}{||\boldsymbol{F}\mathbf{D}_2||}\right) - \frac{\pi}{2}$ represents the angular variation between two fibers in correspondence with a chosen pivot. For the numerical simulations presented hereafter, it was assumed that $\gamma = 2$.

HF2MS: info on Comsol, model implementation, etc.

5.4. Validation of modeling hypotheses

The main assumption of the bidimensional model described in the previous subsection concerned the flatness of transverse cross-sections. For a standard isotropic 3D continuum, Saint Venant solutions prove the existence of so-called anticlastic deformations of cross-sections (Bellow, Ford and Kennedy, 1965). The pantographic blocks were designed in such a way that neither anticlastic nor any other deformation would occur for transverse cross-sections. Such hypothesis is in accordance with the DVC measurements shown in Figures 21-22. It was concluded that the deformation of the transverse surface of the pantographic block was weakly anticlastic. Figure 22 reports that curvature κ_2, which would vanish for synclastic deformation, was slightly negative, thereby producing a Gaussian curvature that was negative as well. This negative value was higher in modulus for the last deflection step, showing that nonlinear effects started playing a more important role. Yet, the curvature κ_2 had a very low value and that this non-zero value was not due to out-of-plane deformations but to microshear of connecting hinges, which allowed for relative sliding at fiber levels that was at the basis of anticlastic deformation. It has to be noted that this effect may be considered negligible in the case under examination and for this reason the 2D model employed for numerical simulations is still valid.

A further validation of the theoretical assumptions is obtained by comparing the displacement fields displayed in Figures 16-17 with the transverse displacement in Figure 18, which was considerably lower than the other two. This result means that cross-sections did not deform much, thus the 2D model may be adopted in the description of the pantographic block.

5.5. Comparison between predicted and measured deformed shapes

Via numerical simulations based on the 2D continuum model described in Equations (5-6), the deformed shapes of a bidimensional continuum corresponding to the pantographic block were computed for the designed 3-point flexural test.

The numerical simulations were carried out using the commercial finite element code Comsol Multiphysics. This software allows a mesh to be produced in an automated manner. The simulations were conducted by implementing the equations underlying the model in weak form. Specifically, the Weak Form module was used, which allows for the minimization of the strain energy written in terms of displacement field variables and their derivatives. The finite elements used for the discretization are of the 5th order (Argyris type), while quadratic Lagrange elements were used to prescribe boundary conditions.

The constitutive parameters were calibrated using the force measurements and taking into account (i) the total number of the pantographic sheets, (ii) the fact that 3D printed materials may have mechanical properties different from the bulk material. The calibrated values for the constitutive parameters K_e, K_b and K_s are as follows

$$K_e^1 = K_e^2 = 6.9 \text{ kN/m}, \qquad K_b^1 = K_b^2 = 4.7 \text{ Nmm}, \qquad K_s = 360 \text{ N/m}. \tag{7}$$

Figure 26 shows a good agreement between the experimental measurements and the predicted reaction forces once the model was calibrated.

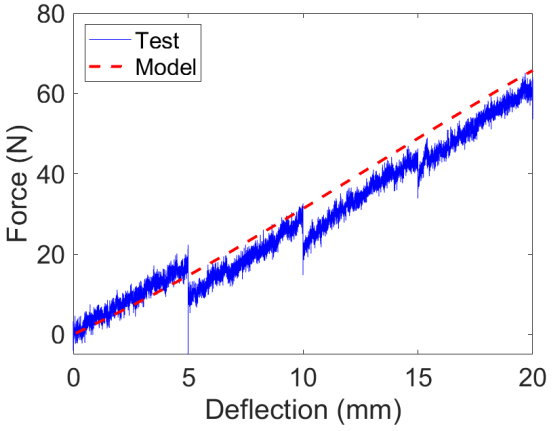

(a)

Figure 26: Comparison between measured and numerically computed reaction forces vs. prescribed deflection

The calibration of the parameters was performed in a qualitative manner. Of course, better parameter identification systems can be implemented and in the case of discrete models this has been done. In the case of the continuum 2D model, the complexity of its implementation implies considerable effort and the creation of a code external to Comsol (e.g. in Matlab) to calibrate the parameters in order to obtain a force-displacement curve in accurate agreement with the experimental one. However, it has been observed that calibrating the parameters only on the force-displacement curve subsequently results in deformed shapes that do not coincide with the experimental ones. This suggests that the quantitative calibration technique must be specially designed and must take multiple factors into account.

In Figures 27-28, the predicted vertical and longitudinal displacement fields are shown. These fields can be compared with those displayed in Figures 16-17, which were measured via DVC. They are in good qualitative agreement. It was concluded that the 2D model was consistent with macroscopic data (*i.e.,* force-deflection curve) and with experimentally measured displacement fields. The adopted 2D model cannot be used for getting predictions analogous to the results of Figure 18, where transverse displacement fields are displayed. For the latter one, the amplitudes were low in comparison to the other two components.

Figures 29-31 show three strain components, namely, ϵ_{xx}, ϵ_{xz} and ϵ_{zz}, where directions x and z were the same as in the DVC frame. Figures 29-30 give a remarkable feature typical of pantographic metamaterials. Due to their

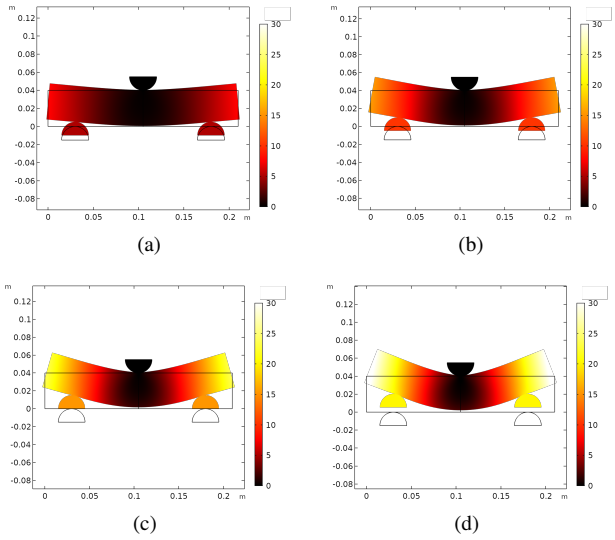

Figure 27: Computed transverse displacement fields on deformed shapes of the pantographic block for different prescribed deflections: (a) 5 mm, (b) 10 mm, (c) 15 mm and (d) 20mm. The displacements are expressed in mm.

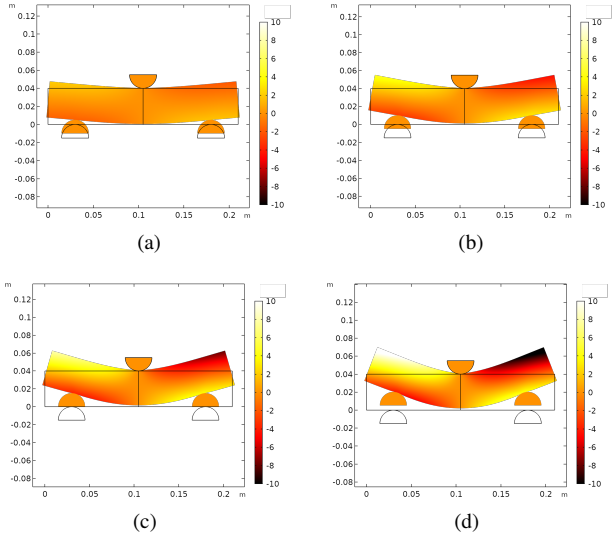

Figure 28: Computed longitudinal displacement fields on the deformed shapes of the pantographic block for different prescribed deflections: (a) 5 mm, (b) 10 mm, (c) 15 mm and (d) 20 mm. The displacements are expressed in mm.

peculiar geometry, the ϵ_{xx} and ϵ_{zz} fields are strongly related. Specifically, an increase in one corresponds to an equal decrease in the other one. Considering the elementary cell of the architecture,*i.e.*, a lozenge whose vertices are replaced by hinges, and assuming approximately that only relative rigid rotations were possible between the four hinged sides, then the diagonals of the lozenge were constrained to vary accordingly. The assumption of rigid rotations may seem restrictive. The mechanics of pantographic metamaterial is much more complex indeed. However, such approximate description allows Figures 29-30 to be interpreted correctly. On close scrutiny, Figure 29 turns out to be the exact opposite of Figure 30.

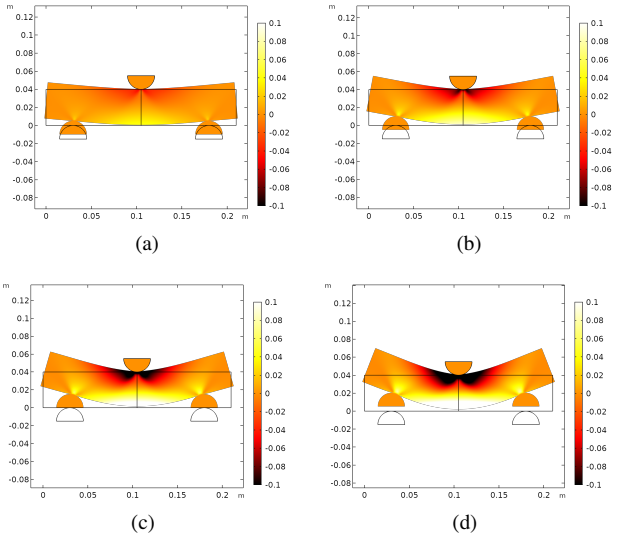

Figure 29: Computed ϵ_{xx} strain fields on deformed shapes of the pantographic block for different prescribed deflections. (a) 5 mm, (b) 10 mm, (c) 15 mm and (d) 20 mm

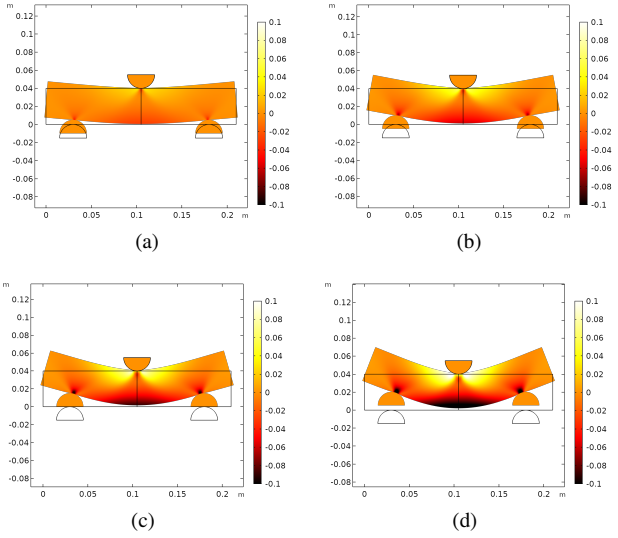

Figure 30: Computed ϵ_{zz} strain fields on deformed shapes of the pantographic block for different prescribed displacement values: (a) 5 mm, (b) 10 mm, (c) 15 mm and (d) 20 mm

The observation of Figure 31 shows that the shear strain ϵ_{xz} was lower in magnitude than the other two components. It was thus concluded that the shear energy played a minor role in this type of test. This conclusion was also drawn by plotting the relative angle change between the two fiber families (Figure 32). As stated in Equation (6), the shear energy was written in terms of angular change.

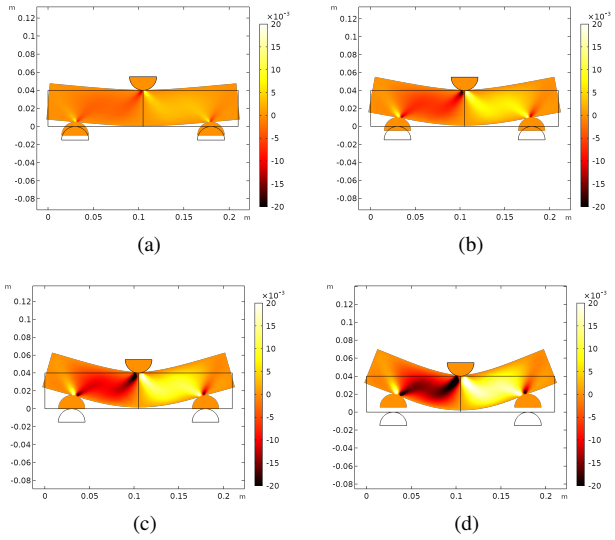

Figure 31: Computed ϵ_{xz} strain field on deformed shapes of the pantographic block for different prescribed displacement values: (a) 5 mm, (b) 10 mm, (c) 15 mm and (d) 20 mm

At the mesostructural level, the previous observation corresponds to the fact that the magnitude of joint torsion remained low. In Figure 32, the rotation fields (corresponding to relative rotation of fibers at the mesostructural level) are shown and only two portions of the specimen exhibited non negligible values. The relative angles between the two fiber families remained almost everywhere equal to 90°. Two portions of the mesostructure, instead, exhibited non-negligible changes of angles. Specifically, there are two portions where changes in the angles are observed. These portions are located in correspondence of the vertical symmetry axis, passing through the support. Due to the fact that the concavity induced by flexure was oriented upward, then the angle between the top fibers increased, while the angle between the bottom fibers decreased. These zones were very localized and a large part of the fibers remained orthogonal even in the deformed configuration. For this reason, the mechanical behavior of the pantographic metamaterial subjected to 3-point flexure was dominated by the flexure of fibers.

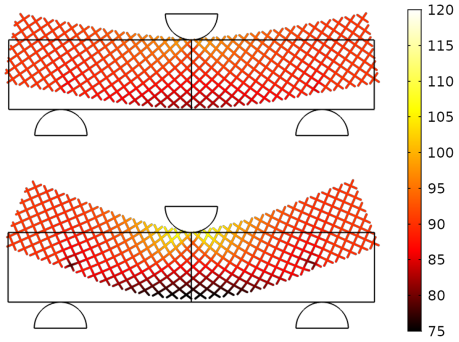

Figure 32: Computed relative angles (in degrees) between the two fiber families for two deflections. (up) 10mm, (down) 20mm.

6. Conclusion

Very few studies were conducted to quantify the deformation of pantographic metamaterials in flexure. In the present case, an *in situ* flexural test was performed. It allowed the metamaterial mesostructure to be imaged for different applied deflections, and kinematic details to be quantified (in particular at the beam and hinge levels) thanks to digital volume correlation (DVC). Such analyses were made possible by using FE-based DVC for which a sub-millimeter mesh, originally constructed on the nominal twin, was fitted to the underlying mesostructure thanks to a backtracking procedure. Given the large displacement amplitudes experienced by the metamaterial, a multi-step initialization was implemented in order to allow mesoscale DVC analyses to converge even under such challenging situation. Since virtually no contrast existed in the solid phase, mechanical regularization was utilized. In the present case, Hencky elasticity was assumed to penalize the DVC cost function with the equilibrium gap cost function. An L-curve criterion was followed to choose the regularization length, which led to the best balance between both cost functions. The analysis of the correlation residual fields showed that convergence was achieved with the selected parameters.

The analysis of the strain fields for the two families of beams showed that they did not deform the same way during the test. Moreover, very high levels were observed close to the external supports, which was a signature of higher order gradient continua. At the hinge level, the displacement and rotation jumps were assessed. It was concluded that the two dominant deformation mechanisms were torsion and shear in comparison to axial contraction and flexure. They led to weakly anticlastic deformations at the macroscale. As evidenced in the present study, a topic of interest for further research is related to the analysis of clasticity of pantographic sheets and blocks. Due to the fact that in this type of metamaterial large deformations and large rotations occur, one should refer to nonlinear shell theories for correctly modeling the mechanical problem (Eremeyev and Zubov, 2007; Eremeyev and Lebedev, 2011; Eremeyev and Altenbach, 2017).

The interest of studying pantographic metamaterials lies in the fact that it requires second gradient homogenized continuum models for its description. It was shown that microstructures call for higher gradient theories in continuum descriptions (Germain, 1973, 2020). Specifically, a 2D planar model for pantographic sheets (dell'Isola et al., 2016) was employed herein for performing numerical simulations validated by experimental measurements. This was possible for a pantographic block due to the fact that the deformations measured via DVC analyses were essentially planar. The numerical simulations were in good agreement with the experiment in terms of reaction force vs. prescribed displacement. Numerical evaluations of displacement fields were shown to be consistent with DVC results.

The study presented herein calls for further experiments. It is necessary to check the emergence of Poisson effects in relation to the aspect ratio of the hinges (*i.e.,* clasticity). Moreover, it may be interesting to study 3-point flexural tests in the transverse direction with respect to that adopted herein. Significantly higher Poisson effects are expected to occur.

7. Acknowledgments

This work has been partially supported by the French "Agence Nationale de la Recherche" through the "Investissements d'avenir" program (ANR-10-EQPX-37 MATMECA Grant). MS was supported by P.O.R. Sardegna F.S.E. 2014-2020 Asse III: Istruzione e Formazione, Obiettivo Tematico: 10, Obiettivo Specifico: 10.5, Azione dell'accordo di Partenariato:10.5.12 - Avviso di chiamata per il finanziamento di Progetti di ricerca, Anno 2017 (CUP F24J17000190009).

References

Alibert, J.J., Seppecher, P., dell'Isola, F., 2003. Truss modular beams with deformation energy depending on higher displacement gradients. Mathematics and Mechanics of Solids 8, 51–73.

Auffray, N., dell'Isola, F., Eremeyev, V.A., Madeo, A., Rosi, G., 2015. Analytical continuum mechanics à la Hamilton–Piola least action principle for second gradient continua and capillary fluids. Mathematics and Mechanics of Solids 20, 375–417.

Auger, P., Lavigne, T., Smaniotto, B., Spagnuolo, M., dell'Isola, F., Hild, F., 2021. Poynting Effects in Pantographic Metamaterial Captured via Multiscale DVC. Journal of Strain Analysis for Engineering Design 56(7), 462–477.

Barchiesi, E., Eugster, S.R., Placidi, L., dell'Isola, F., 2019. Pantographic beam: a complete second gradient 1D-continuum in plane. Zeitschrift für angewandte Mathematik und Physik 70, 1–24.

Bay, B., 2008. Methods and applications of digital volume correlation. Journal of Strain Analysis for Engineering Design 43, 745–760.

Bay, B., Smith, T., Fyhrie, D., Saad, M., 1999. Digital volume correlation: three-dimensional strain mapping using X-ray tomography. Experimental Mechanics 39, 217–226.

Bellow, D.G., Ford, G., Kennedy, J., 1965. Anticlastic behavior of flat plates. Experimental Mechanics 5, 227–232.

Boutin, C., dell'Isola, F., Giorgio, I., Placidi, L., 2017. Linear pantographic sheets: asymptotic micro-macro models identification. Mathematics and Mechanics of Complex Systems 5, 127–162.

Buffière, J., Maire, E., Adrien, J., Masse, J., Boller, E., 2010. In Situ Experiments with X ray Tomography: an Attractive Tool for Experimental Mechanics. Experimental Mechanics 50, 289–305.

Buljac, A., Jailin, C., Mendoza, A., Neggers, J., Taillandier-Thomas, T., Bouterf, A., Smaniotto, B., Hild, F., Roux, S., 2018. Digital Volume Correlation: Review of Progress and Challenges. Experimental Mechanics 58, 661–708.

Ciallella, A., Pasquali, D., Gołaszewski, M., D'Annibale, F., Giorgio, I., 2021. A rate-independent internal friction to describe the hysteretic behavior of pantographic structures under cyclic loads. Mechanics Research Communications 116, 103761–1–5.

Cuomo, M., dell'Isola, F., Greco, L., Rizzi, N., 2017. First versus second gradient energies for planar sheets with two families of inextensible fibres: investigation on deformation boundary layers, discontinuities and geometrical instabilities. Composites Part B: Engineering 115, 423–448.

dell'Isola, F., Giorgio, I., Pawlikowski, M., Rizzi, N.L., 2016. Large deformations of planar extensible beams and pantographic lattices: heuristic homogenization, experimental and numerical examples of equilibrium. Proceedings of the Royal Society A: Mathematical, Physical and Engineering Sciences 472, 20150790–1–23.

dell'Isola, F., Seppecher, P., Alibert, J.J., Lekszycki, T., Grygoruk, R., Pawlikowski, M., Steigmann, D., Giorgio, I., Andreaus, U., Turco, E., Gołaszewski, M., et al., 2019a. Pantographic metamaterials: an example of mathematically driven design and of its technological challenges. Continuum Mechanics and Thermodynamics 31, 851–884.

dell'Isola, F., Seppecher, P., Spagnuolo, M., Barchiesi, E., Hild, F., Lekszycki, T., Giorgio, I., Placidi, L., Andreaus, U., Cuomo, M., Eugster, S., Pfaff, A., Hoschke, K., Langkemper, R., Turco, E., Sarikaya, R., Misra, A., De Angelo, M., D'Annibale, F., Bouterf, A., Pinelli, X., Misra, A., Desmorat, B., Pawlikowski, M., Dupuy, C., Scerrato, D., Peyre, P., Laudato, M., Manzari, L., Göransson, P., Hesch, C., Hesch, S., Franciosi, P., Dirrenberger, J., Maurin, F., Vangelatos, Z., Grigoropoulos, C., Melissinaki, V., Farsari, M., Muller, W., Abali, E., Liebold, C., Ganzosch, G., Harrison, P., Drobnicki, R., Igumnov, L., Alzahrani, F., Hayat, T., 2019b. Advances in Pantographic Structures: Design, Manufacturing, Models, Experiments and Image Analyses. Continuum Mechanics and Thermodynamics 31, 1231–1282.

Desmorat, B., Desmorat, R., 2008. Topology optimization in damage governed low cycle fatigue. Comptes Rendus Mécanique 336, 448–453.

Eremeyev, V., Altenbach, H., 2017. Basics of mechanics of micropolar shells, in: Altenbach, H., Eremeyev, V. (Eds.), Shell-like Structures: Advanced Theories and Applications. Springer, Cham, pp. 63–111.

Eremeyev, V., Lebedev, L., 2011. Existence theorems in the linear theory of micropolar shells. ZAMM - Journal of Applied Mathematics and Mechanics / Zeitschrift für Angewandte Mathematik und Mechanik 91, 468–476.

Eremeyev, V., Zubov, L., 2007. On constitutive inequalities in nonlinear theory of elastic shells. ZAMM - Journal of Applied Mathematics and Mechanics / Zeitschrift für Angewandte Mathematik und Mechanik 87, 94–101.

Franciosi, P., 2020. Uniformity of the Green operator and Eshelby tensor for hyperboloidal domains in infinite media. Mathematics and Mechanics of Solids 25, 1610–1642.

George, D., Allena, R., Remond, Y., 2018. A multiphysics stimulus for continuum mechanics bone remodeling. Mathematics and Mechanics of Complex Systems 6, 307–319.

Germain, P., 1973. The method of virtual power in continuum mechanics. Part 2: Microstructure. SIAM Journal on Applied Mathematics 25, 556–575.

Germain, P., 2020. The method of virtual power in the mechanics of continuous media, I: Second-gradient theory. Mathematics and Mechanics of Complex Systems 8, 153–190.

Giorgio, I., 2016. Numerical identification procedure between a micro-Cauchy model and a macro-second gradient model for planar pantographic structures. Zeitschrift für angewandte Mathematik und Physik 67, 1–17.

Giorgio, I., 2021. Lattice shells composed of two families of curved Kirchhoff rods: an archetypal example, topology optimization of a cycloidal metamaterial. Continuum Mechanics and Thermodynamics 33, 1063–1082.

Giorgio, I., dell'Isola, F., Andreaus, U., Alzahrani, F., Hayat, T., Lekszycki, T., 2019. On mechanically driven biological stimulus for bone remodeling as a diffusive phenomenon. Biomechanics and modeling in mechanobiology 18, 1639–1663.

Giorgio, I., Varano, V., dell'Isola, F., Rizzi, N.L., 2021. Two layers pantographs: a 2D continuum model accounting for the beams' offset and relative rotations as averages in SO (3) Lie groups. International Journal of Solids and Structures 216, 43–58.

Greco, L., Giorgio, I., Battista, A., 2017. In plane shear and bending for first gradient inextensible pantographic sheets: numerical study of deformed shapes and global constraint reactions. Mathematics and Mechanics of Solids 22, 1950–1975.

Hansen, P., 2000. The L-Curve and its Use in the Numerical Treatment of Inverse Problems, in: P. Johnston (Ed.) Computational Inverse Problems in Electrocardiology, Advances in Computational Bioengineering, pp. 119–142.

Hild, F., Bouterf, A., Chamoin, L., Mathieu, F., Neggers, J., Pled, F., Tomičević, Z., Roux, S., 2016. Toward 4D Mechanical Correlation. Advanced Modeling and Simulation in Engineering Sciences 3, 1–26.

Kleinendorst, S., Hoefnagels, J., Geers, M., 2019. Mechanical Shape Correlation: A novel integrated digital image correlation approach. Computer Methods in Applied Mechanics and Engineering 345, 983–1006.

Leclerc, H., Neggers, J., Mathieu, F., Hild, F., Roux, S., 2015. Correli 3.0. IDDN.FR.001.520008.000.S.P.2015.000.31500. Agence pour la Protection des Programmes, Paris (France).

Leclerc, H., Périé, J., Hild, F., Roux, S., 2012. Digital volume correlation: What are the limits to the spatial resolution? Mechanics & Industry 13, 361–371.

Luscher, D.J., McDowell, D.L., Bronkhorst, C.A., 2010. A second gradient theoretical framework for hierarchical multiscale modeling of materials. International Journal of Plasticity 26, 1248–1275.

Maati, A., Tabourot, L., Balland, P., Belaid, S., 2020. Influence of the material microstructural properties on a 3-point bending test. Mechanics & Industry 21, 518–1–9.

Maire, E., Withers, P.J., 2014. Quantitative X-ray tomography. International Materials Reviews 59, 1–43.

Mindlin, R.D., 1965. Second gradient of strain and surface-tension in linear elasticity. International Journal of Solids and Structures 1, 417–438.

Patil, S., Ravi, B., 2005. Voxel-based representation, display and thickness analysis of intricate shapes, in: Ninth International Conference on Computer Aided Design and Computer Graphics (CAD-CG'05), p. 6 pp.

Pfaff, A., Bierdel, M., Hoschke, K., Wickert, M., Riedel, W., Hiermaier, S., 2020. Resource analysis model and validation for selective laser melting, constituting the potential of lightweight design for material efficiency. Sustainable Production and Consumption 21, 182–191.

Pideri, C., Seppecher, P., 1997. A second gradient material resulting from the homogenization of an heterogeneous linear elastic medium. Continuum Mechanics and Thermodynamics 9, 241–257.

Placidi, L., Andreaus, U., Giorgio, I., 2017. Identification of two-dimensional pantographic structure via a linear D4 orthotropic second gradient elastic model. Journal of Engineering Mathematics 103, 1–21.

Roux, S., Hild, F., Viot, P., Bernard, D., 2008. Three dimensional image correlation from X-Ray computed tomography of solid foam. Composites Part A: Applied Science and Manufacturing 39, 1253–1265.

Schaedler, T., Carter, W., 2016. Architected cellular materials. Annual Review of Materials Research 46, 187–210.

Schulte, J., Dittmann, M., Eugster, S., Hesch, S., Reinicke, T., dell'Isola, F., Hesch, C., 2020. Isogeometric analysis of fiber reinforced composites using Kirchhoff–Love shell elements. Computer Methods in Applied Mechanics and Engineering 362, 112845–1–34.

Spagnuolo, M., 2020. Circuit analogies in the search for new metamaterials: Phenomenology of a mechanical diode, in: Altenbach H., Eremeyev V., Pavlov I., Porubov A. (eds) Nonlinear Wave Dynamics of Materials and Structures. Advanced Structured Materials, vol 122. Springer, Cham, Swizerland, pp. 411–422.

Spagnuolo, M., Andreaus, U., Misra, A., Giorgio, I., Hild, F., 2021. Mesoscale modeling and experimental analyses for pantographic cells: effect of hinge deformation. Mechanics of Materials 160, 103924–1–11.

Spagnuolo, M., Barcz, K., Pfaff, A., dell'Isola, F., Franciosi, P., 2017. Qualitative pivot damage analysis in aluminum printed pantographic sheets: Numerics and experiments. Mechanics Research Communications 83, 47–52.

Spagnuolo, M., Cazzani, A.M., 2021. Contact interactions in complex fibrous metamaterials. Continuum Mechanics and Thermodynamics 33, 1873–1889.

Spagnuolo, M., Peyre, P., Dupuy, C., 2019. Phenomenological aspects of quasi-perfect pivots in metallic pantographic structures. Mechanics Research Communications 101, 103415–1–6.

Spagnuolo, M., Yildizdag, M.E., Pinelli, X., Cazzani, A., Hild, F., 2022. Out-of-plane deformation reduction via inelastic hinges in fibrous metamaterials and simplified damage approach. Mathematics and Mechanics of Solids 27, 1011–1031.

Sutton, M., 2013. Computer vision-based, noncontacting deformation measurements in mechanics: A generational transformation. Applied Mechanics Reviews 65, 050802–1–23.

Taillandier-Thomas, T., Roux, S., Morgeneyer, T., Hild, F., 2014. Localized strain field measurement on laminography data with mechanical regularization. Nuclear Instruments and Methods in Physics Research Section B 324, 70–79.

Turco, E., dell'Isola, F., Cazzani, A., Rizzi, N., 2016. Hencky-type discrete model for pantographic structures: numerical comparison with second gradient continuum models. Zeitschrift für angewandte Mathematik und Physik 67, 1–28.

Valmalle, M., Vintache, A., Smaniotto, B., Gutmann, F., Spagnuolo, M., Ciallella, A., Hild, F., 2022. Local-global DVC analyses confirm theoretical predictions for deformation and damage onset in torsion of pantographic metamaterial. Mechanics of Materials 172, 104379.

Yang, H., Ganzosch, G., Giorgio, I., Abali, B.E., 2018. Material characterization and computations of a polymeric metamaterial with a pantographic substructure. Zeitschrift für angewandte Mathematik und Physik 69, 1–16.

Yang, Y., Misra, A., 2012. Micromechanics based second gradient continuum theory for shear band modeling in cohesive granular materials following damage elasticity. International Journal of Solids and Structures 49, 2500–2514.

Appendix: DVC hardware and analyses parameters

Table 1
DVC hardware parameters

Tomograph	North Star Imaging X50+
X-ray source	XRayWorX XWT-240-CT
Target / Anode	W (reflection mode)
Filter	none
Voltage	120 kV
Current	170 µA
Focal spot size	5 µm
Tube to detector	771.4 mm
Tube to object	514.1 mm
Detector	Dexela 2923
Definition	1536×1944 pixels (2×2 binning)
Number of projections	1500
Angular amplitude	360°
Frame average	5 per projection
Frame rate	5 fps
Acquisition duration	44 min 14 s
Reconstruction algorithm	filtered back-projection
Gray Levels amplitude	16 bits
Volume size	$620 \times 1850 \times 880$ voxels (after crop)
Field of view	$62.0 \times 185.0 \times 88.0$ mm^3 (after crop)
Image scale	100 µm/voxel

Table 2
DVC analysis parameters

DIC software	Correli 3.0 (Leclerc et al., 2015)
Image filtering	none
Element length (mean)	6 vx (or 0.6 mm)
Shape functions	linear (T4 elements (Hild et al., 2016))
Mesh	see Figure 9
Matching criterion	penalized sum of squared differences
Regularization length	$\ell_m = 25$ vx (or 2.5 mm)
Interpolant	cubic
Displacement noise floor	see Figure 10(a)
Strain noise floor	see Figure 10(b)